GEOMETRIC AND NUMERICAL MODELING FOR POROUS MEDIA WAVE PROPAGATION

D. Uribe
M. Osorno
CAD/CAM/CAE Laboratory
Universidad EAFIT
Institute of Mechanics
Ruhr-University Bochum
duribega,mosornot@eafit.edu.co

H. Steeb
Institute of Mechanics
Ruhr-University Bochum
holger.steeb@rub.de

E. H Saenger
Geological Institute
ETH Zürich
erik.saenger@ethz.ch

O. Ruiz
CAD/CAM/CAE Laboratory
Universidad EAFIT
oruiz@eafit.edu.co

ABSTRACT

Determining hydro-mechanical properties of porous materials present a challenge because they exhibit a more complex behaviour than their continuous counterparts. The geometrical factors such as pore shape, length scale and occupancy play a definite role in the materials characterization. On the other hand, computational mechanics calculations for porous materials face an intractable amount of data. To overcome these difficulties, this investigation propose a workflow (Image segmentation, surface triangulation and parametric surface fitting) to model porous materials (starting from a high-resolution industrial micro-CT scan) and transits across different geometrical data (voxel data, cross cut contours, triangular shells and parametric quadrangular patches) for the different stages in the computational mechanics simulations. We successfully apply the proposed workflow in aluminum foam. The various data formats allow the calculation of the tortuosity value of the material by using viscoelastic wave propagation simulations and poroelastic investigations. Future work includes applications for the geometrical model such as boundary elements and iso-geometrical analysis, for the calculation of material properties.

KEYWORDS

Computational mechanics, geometric modeling, porous materials, wave propagation.

NOMENCLATURE

$G = (\mathbf{P}, E)$	=	Graph with vertex set $\mathbf{P}$ and edge set E, nearly embedded in S_0
P	=	Pressure scalar field of a fluid occupying Ω. $P : \Omega \to \mathbb{R}$.
S_0	=	2-manifold (possibly disconnected, with border) surface corresponding to the isosurface $V(p) = V_{TR}$ for $p \in \Omega$.
T	=	$\{t_1, t_2, \ldots\}$ triangular mesh of triangles t_i with vertices in $\mathbf{P}$
V	=	A scalar field $V : \Omega \to \mathbb{R}$ produced by the CT scan of Aluminum Foam in Ω.
V_{TR}	=	Threshold real value in Hounsfield units which marks the presence of Aluminum Foam in a CT scan.
Ω	=	Rectangular prism aligned with the world axes such that $\Omega \subset \mathbb{R}^3$.

1. INTRODUCTION

Micro-scale Computational Mechanics studies of porous media are limited by the difficulty in geometrically modelling the microstructure material in an accurate manner. The cavities are extremely small, the data size is very significant, and the data is present in unusable formats, since (e.g.) Voxel-based geometries cannot be used in most commercial structural mechanics and computational fluid dynamics software.

Researchers take two approaches: (i) Create their own geometries, based on abstraction of the subscale geometries. Examples are the so called 'packed spheres', lattices from convex uniform honeycombs, boolean operations with spheres or ellipsoids, Gaussian random fields, among others ([8], [19]). (ii) Use actual scan samples of porous media geometries that are based on CT scan data, which favors the usage of regular grid numerical methods. These methods have shortcomings in imposing boundary conditions, dealing with high frequency saw-tooth geometries, and describing curved boundaries with large numbers of degrees of freedom.

In this article we implement and apply several geometrical processing methods to represent solids from industrial micro CT scans of porous materials. The different representations of the material (voxels, contours, triangular meshes and parametric surfaces), allow simulations in the middle steps of the process. We can also manage the information about the porous media geometry with a lower memory usage. Finally with the parametric surfaces of the material, is possible the use of robust commercial CAE software that can not manage voxel-based information.

The workflow of our method begins by processing the micro-CT scan data using image segmentation algorithms (multiple thresholding, watershed algorithms). The segmented data represents enumerations, 3D scalar fields and planar cross sections, which are used to build 3D shell and solid information by using several algorithms: Marching Cubes, Poisson, 2-D similarity Voronoi- Delaunay generalized lofting, Power Crust and Surface Optimization. Parallelized computations have been applied, using as a unit cubic sub-domains of the general domain.

We have successfully created the enumeration, cross sectional, triangular and parametric representation of aluminum foam. From those representations, it was possible to estimate geometric properties, such as: porosity, lattice cross sectional area and shapes, and pore radius. The geometric properties were used on analytical solutions of wave propagation in porous media and compared with independent numerical simulations. The tortuosity is estimated, using the Geometrical Scenario formed, in two manners: Using Biot's poroelastic approach (a) The flow velocity is calculated and from it, the tortuosity. (b) Virtually stiffening the aluminium foam, calculating the flow velocity and from it the tortuosity. The results closely match each other.

This paper is organized as follows: Section 2 reviews the literature existent on the geometrical modeling of materials with micro-structure. Section 3 explains the various geometrical methods aligned to model the porous materials. Section 4 discusses computational mechanics methods mounted on the geometrical models, presenting the achieved results on mechanical properties and performance. Section 5 concludes the article and enumerates open research areas.

2. LITERATURE REVIEW

The reconstruction of surface and solid from CT-data is a common problem in computational geometry and visualization, but authors usually only focus in a specific part of the workflow: 1) Image segmentation, 2) Surface triangulation, 3) Parametric surface fitting.

Wirjardi ([30]) exposes a survey on the more common techniques for image segmentation, such as thresholding ([17], [27]), region growing ([1]) and deformable surfaces ([5]). Usually additional techniques are applied to correct noise and other data adquisition defects. Iassonov, et al. ([11]) proposes Image Analysis Normalization for image correction.

Several authors have proposed methods for surface triangulation from image segmented data. Lorensen et al. ([15]) propose an algorithm (Marching cubes) that generate a triangulation from voxels data employing a table of edge intersections. Amenta et al. ([2]) propose the Power crust algorithm which generates a triangulated mesh form a point set data. The obtained result does not depend on the data quality, but has the disvantage that only works with surface points. Ruiz et al. ([21]) recover a triangulated surface from slice samples by using 2D shape similarity. This method can be used when a topological faithfulness is really needed, but implies pre-processing to obtain 2D slices from the CT-scan data.

Different methods have also been proposed for generate parametric surfaces from points clouds or meshes.

Kazhdan et al. ([13]) solve the problem of generating surfaces form a point data set treating it like the solution of Poisson equation. A good detail level is possible but the input data set must have ordered points. Ruiz et al. ([22]) present a stochastic approach to surface reconstruction from noisy points data set based on Principal Component Analysis, which has a good behaviour with non self-intersecting curves. Other proposed methods for generating parametric surfaces can be seen in [6], [12] and [18].

The reviewed methods present some disadvantages as restriction in the input data and high computational requirements. In this paper we propose a workflow for applying more efficient methods to obtain a geometrical model that can be used suitably for numerical simulation of effective material properties.

3. METHODOLOGY

Consider a domain $\Omega \subset \mathbb{R}^3$ forming a rectangular prism aligned with the axes of $\mathbb{R}^3$. The domain Ω contains a porous material. A computer tomogram of Ω results in a scalar field $V : \Omega \to \mathbb{R}$ which corresponds to the absorption of the X-rays by the material, measured in Hounsfield units. The CT scanner used has a resolution of 60 micrometers / Voxel.

In the present case the analysed porous material is 10 ppi AlSi7Mg foam (Fig. 1) by m.pore GmbH. Tab. 1 shows the modelling parameters of the aluminum foam.

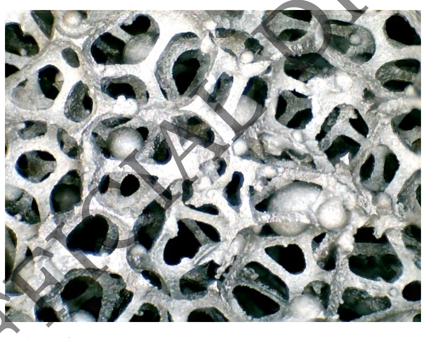

Figure 1 Aluminum Foam.

The goal of this section is to describe the different algorithms used in this investigation to obtain explicit representations of S_{TR}., suitable for numerical calculations of effective hydro-mechanical properties.

3.1. Iso-Surface Occupancy

- **Given:**
  1. A scalar field $V : \Omega \to \mathbb{R}$.
  2. A real (threshold) value V_{TR} in the range of V.
- **Goal:**
  1. T triangulation approximating $V(p) = V_{TR}$ for $p \in \Omega$.

This part of the process is conducted by using a variation of the Marching Cubes algorithm ([15]). The triangulation T must have the characteristics of 2-manifoldness. Notice that $T \approx S_0$ has borders and it is possibly disconnected within Ω.

3.2. Cross-section-based Surface Reconstruction

Iso-Curve Occupancy

- **Given:**
  1. A slice k-th of the CT scan in plane Π_k with normal Z.
  2. A real (threshold) value V_{TR} in the range of V.
- **Goal:**
  1. A set $\partial V \cup_k = \{\Gamma_0, \Gamma_1, ...\}$ of closed contours Γ_j , $j = 0, 1, ...$ on Π_k, which compose the boundary $\partial V \cup_k$ of the set $V \cup_k = \{p \in \Pi_k | V(p) \geq V_{TR}\}$.

Fig. 2(a) shows a typical slice Π_k of the CT scan. Each pixel (i, j) of the Π_k slice corresponds to the point $(x_i, y_j, z_k) \in \Omega \subset \mathbb{R}^3$. Fig. 2(a) displays the pixels with $V(x_i, y_j, z_k) \geq V_{TR}$. Each pixel represents a diminute square inside Π_k., and the 2D boolean union of pixels inside the foam results in a 2D region with city-block jagged boundary $\partial V \cup$ in Fig.2(b). A smoothing of these jagged contours using a Catmull-Rom interpolation produces the smooth contours in Fig. 2(c). Since the foam may have internal disconnected cavities, the cross sections $V \cup$ of the foam present holes, and their boundary ∂VU has several disconnected components ($\partial V \cup = \{\Gamma_0, \Gamma_1\}$). In our discussion, Γ_0 represents an external foam contour and Γ_i for $i = 1, 2, ...$ represent the internal contours. The collection of such cross sections for a particular neighborhood of Ω is shown in Fig. 3(a).

If the distance between scan planes is considered, volumetric pixels (Voxels) are formed, which correspond to the parts of Ω filled by the aluminum foam (Fig. 3(b)).

2D-similarity-driven Voronoi-Delaunay Algorithm

- **Given:**
  1. A sequence of parallel cross sections of the domain Ω, Π_k with $k = 1, 2, ...$

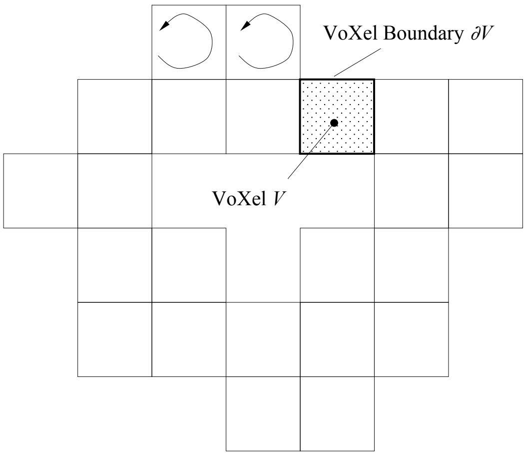

(a) Set of Voxels with 6000 above threshold.

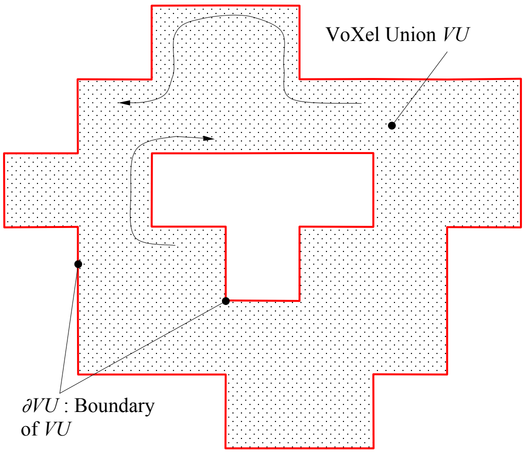

(b) Boolean Union of Voxels. City Block Contours.

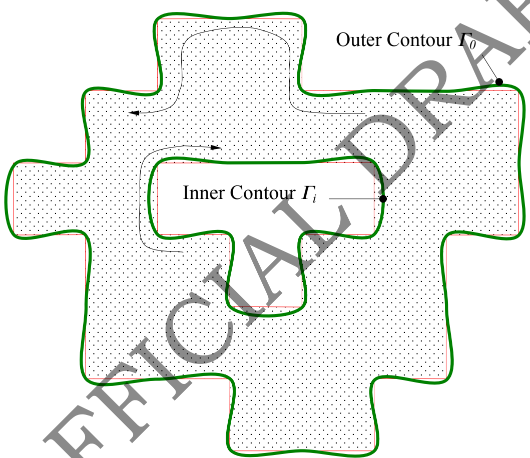

(c) Catmull-Rom smoothing of City Block Contours.

Figure 2 Contour Construction from CT Voxel per-slice Data.

2. A set $\partial V\cup_k = \{\Gamma_0, \Gamma_1, ...\}$ of closed contours Γ_j , $j = 0, 1, ...$ on Π_k, which compose the boundary $\partial V\cup_k$ of the set $V\cup_k = \{p \in \Pi_k | V(p) \geq V_{TR}\}$.

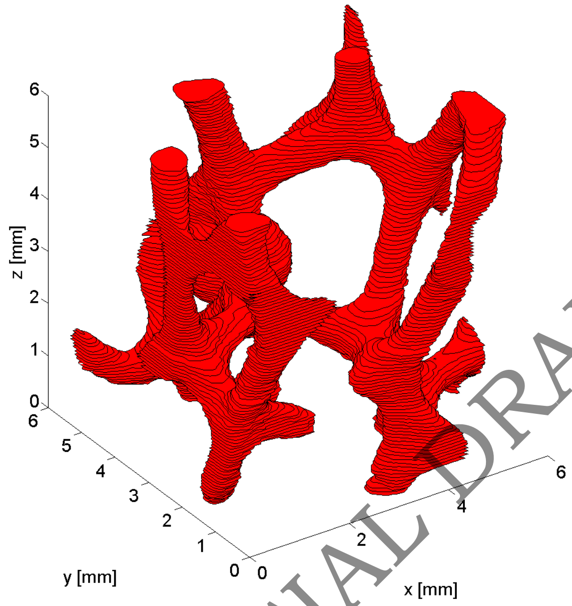

(a) Lattice Contours

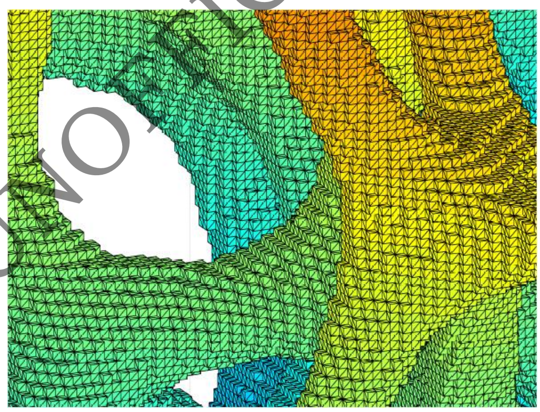

(b) Volumetric Pixels (VoXels) in CT Scan.

Figure 3 Contours per-slice and Voxels.

- **Goal:**
  1. A sequence of triangular mesh surfaces $T_{i,i+1}$ that map the contours $\partial V\cup_i$ of level Π_i, onto the contours $\partial V\cup_{i+1}$ of level Π_{i+1}.
  2. T triangulation approximating the iso-surfaces $V(p) = V_{TR}$ for $p \in \Omega$. Notice that $T = \cup_i T_{i,i+1}$.

The triangular mesh that materializes the mapping among contours of consecutive slices is calculated by algorithms discussed in [21] or [4] and produces the results in Fig. 4. The mapping among contours (i.e lofting) may have a strictly local proximity criterion (Voronoi - Delaunay methods, [4]) or it may have a topological and 2D - shape similarity rationale that

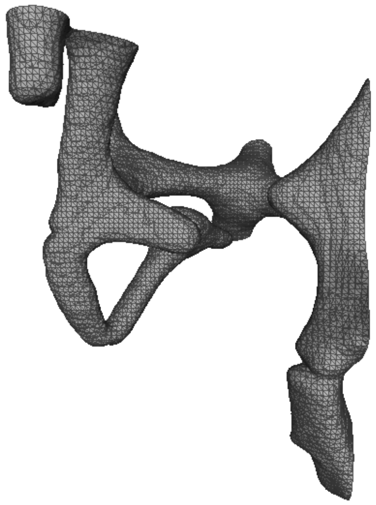

(a) View 1.

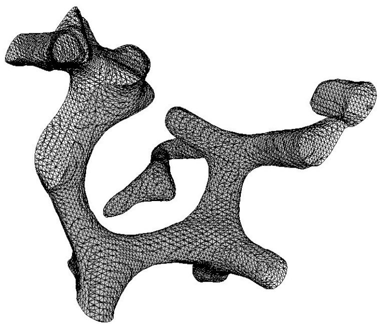

(b) View 2.

Figure 4 Triangular Mesh Surfaces formed by Contour-mapping (generalized lofting [4, 21]) between Consecutive Cross Section Contour Sets.

selectively triggers the V-D methods ([21]). The topological and 2D shape similarity methods use the fact that topological evolution of features along the cross sections obeys to only 3 topological transitions ([16]). A topological event corresponds to the addition of one of: 0-handle, 1-handle or 2-handle, to the previous contour, and causes the number of contours to change from cross section Π_i to cross section Π_{i+1}. Fig. 5 shows that the number of contours in slice Π_i will have a variation of +1, -1, +1, -1 as a consequence of the addition of 0-handle, 1-handle, 1-handle and 2-handle, respectively.

3.3. Triangular Mesh to Parametric Surfaces

- **Given:**

  1. T triangulation approximating the iso-surfaces $V(p) = V_{TR}$ for $p \in \Omega$.

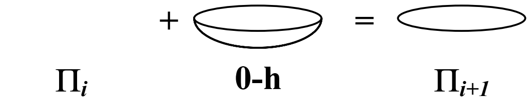

(a) 0-handle addition.

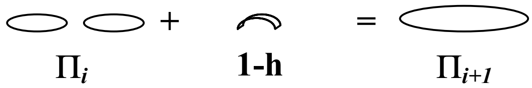

(b) 1-handle addition.

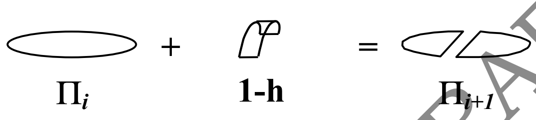

(c) 1-handle addition.

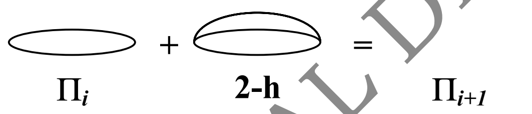

(d) 2-handle addition.

Figure 5 Topological Transitions as k-Handle Additions ([21].

- **Goal:**

  1. A Set of parametric patches $S_j(u, w)$ which approximate the triangular mesh T so that $\cup_j S_j(u, w) \approx T = \cup_i T_{i,i+1}$.

In [20] an algorithm is reported, which uses the graph T under a point sample as proximity graph in Manifold Learning Algorithms. The parametric surfaces fit to the triangular mesh appear in Figs. 6(a) and 6(b).

4. RESULTS AND DISCUSSION

4.1. Aluminium Foam geometrical modeling

Fig. 2(a) shows a slice of the CT scan, which corresponds to the pixels with $V(x, y, z) \geq V_{TR}$. The 2D boolean union of such pixels results in a city-block jagged boundary in Fig.2(b). If the distance between scan planes is considered, Volumetric Pixels (Voxels) are formed, which correspond to the parts of Ω filled by the Aluminum Foam (Fig. 3(b)). A smoothing of these jagged contours produced with a Catmull-Rom interpolation produces the results in Fig. 2(c). The collection of such cross sections for a particular neighborhood of Ω is shown in Fig. 3(a). The generalized lofting among cross sections produces triangular shells, shown in Fig. 4. The parametric surfaces fit to the triangular mesh appear in Figs. 6(a) and 6(b).

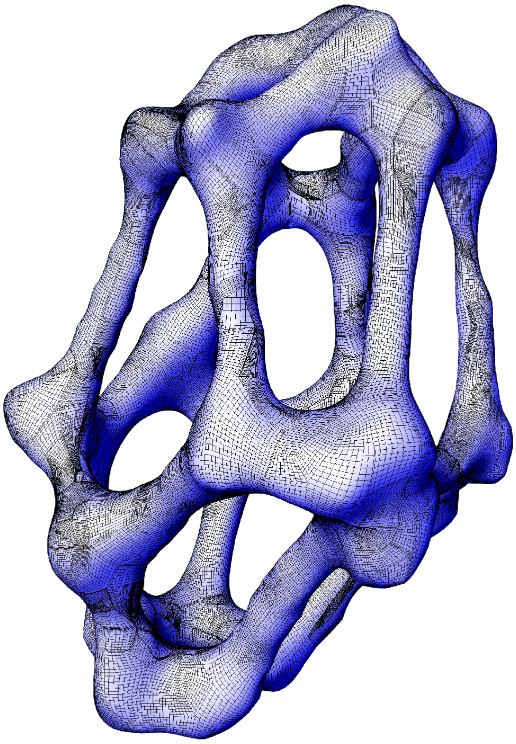

(a) Sub-domain

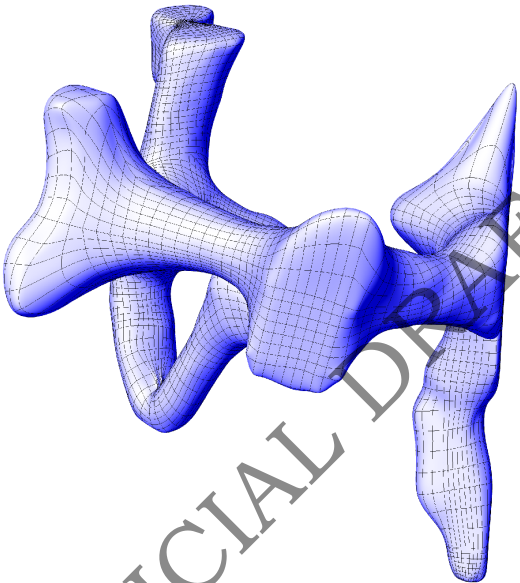

(b) Surface Modeling of Subdomain.

Figure 6 Parametric surfaces of the geometric modeling of the aluminum foam.

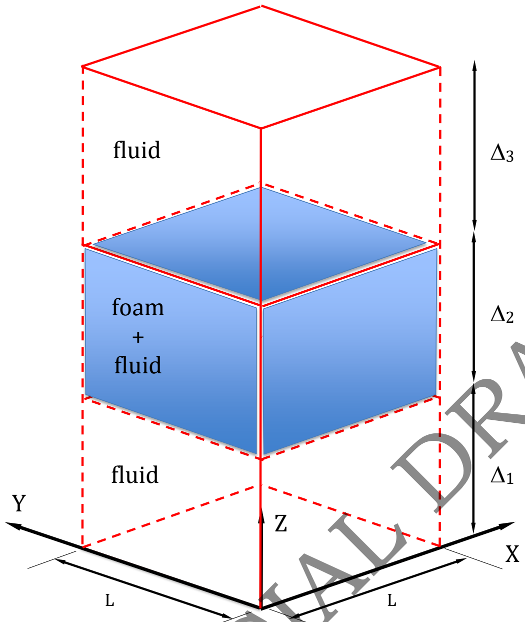

(a) Fluid and Foam-Fluid Domains Ω.

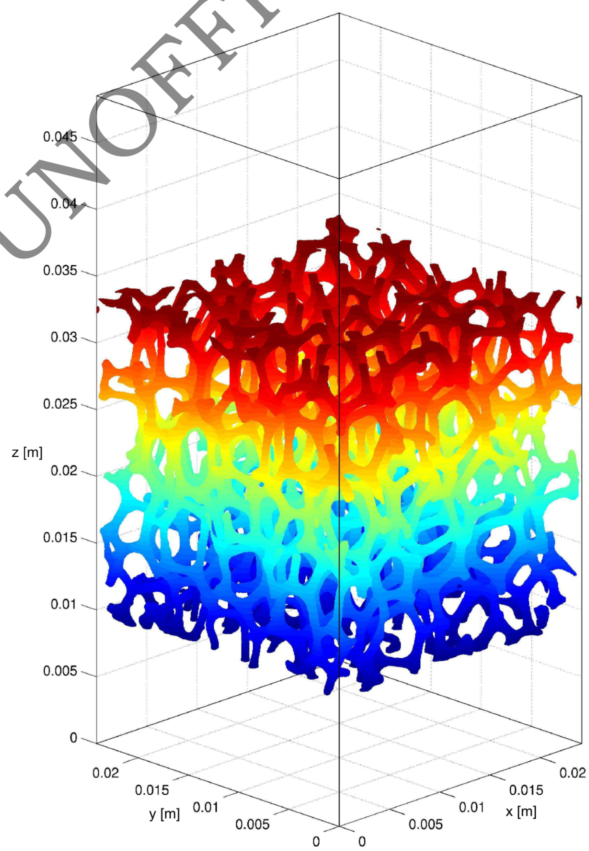

(b) Foam Domain Ω_2

Figure 7 Experimental Set-Up

4.2. Experimental Set-Up

Consider a domain $\Omega \subset \mathbb{R}^3$ (Fig. 7(a)) open in the planes $z = 0$ and $z = L$ and closed in the sides (planes $x = 0$, $x = L$, $y = 0$, $y = L$). The boundary of the domain $\partial\Omega$, allows free pass of fluid in the planes $x = 0$ and $x = L$ and is hermetic in the planes $x = 0$, $x = L$, $y = 0$ and $y = L$. Ω is divided in 3 slices, as follows: (1) Ω_1, with $0 \leq z \leq \Delta_1$, filled with a viscous pore fluid. (2) Ω_2, with $\Delta_1 \leq z \leq \Delta_1 + \Delta_2$, filled with

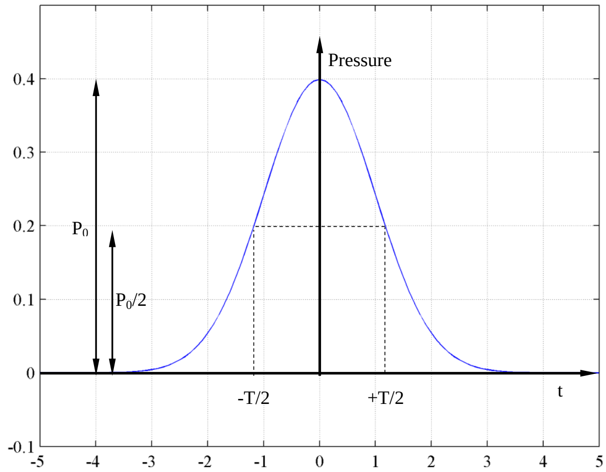

Figure 8 Pressure Wave

metallic foam whose interstices are filled by the fluid. (3) Ω_3, with $\Delta_1+\Delta_2 \leq z \leq \Delta_1+\Delta_2+\Delta_3$, filled with the fluid. There are no obstacles for the movement of the fluid in the Z direction, except the presence of the aluminum foam itself.

At the plane $z = 0$ an acoustic wave excites the medium in direction perpendicular to the plane with an ultrasonic transducer. The wave is described in the frequency domain by a Gaussian distribution $\mathcal{N}(0, f_c)$. The value f_c will indicate whether the propagating wave is in Biot's high or low frequency domain, cf. discussion in [14]. It is of our interest to calculate Biot's high frequency limit, since the viscous effects of the fluid can be neglected, and the complexity of the constitutive equation of the fluid is significantly simpler. In order to enforce this, the value of the central frequency of the propagating wave must be significantly greater than Biot's critical frequency. From this experimental set-up, two pressure waves are numerically obtained (slow and fast P-wave, cf. [3] , and then any missing material parameter in Biot's equation can be calculated (e.g. tortuosity).

$$f_{crit} = \frac{\eta}{\pi \rho^{fR} r^2} \tag{1}$$

The calculation of Biot's critical frequency f_{crit} is calculated using the pore radius r found from the parametric surfaces in section 3.3. It is found that f_{crit} is smaller than 1 Hz. Therefore a wave with a central frequency of 24 KHz lies in the high frequency domain. To record the interaction of the wave with the water saturated foam, seismographs are placed in the planes $z = \Delta_1$ and $z = \Delta_1+\Delta_2$. The material parameters for the water phase and the aluminum phase can be found in Tab. 1.

Young's modulus of aluminium	E^s = 70.0 GPa
Poisson number of aluminium	ν^s = 0.33
Density of aluminium	ρ^{sR} = 2700 kg/m^3
Bulk modulus of water	K^f = 1.48 GPa
Density of water	ρ^{fR} = 1000 kg/m^3
P-wave velocity of water	$V_{p,water}$ = 1480 m/s

Table 1 Modeling parameters of the fluid and solid phases

In order to simulate the experimental setup, the momentum equation is solved using a Rotated Staggered Grid Finite Differences scheme (RSG-FD)([24, 25, 29]). The RSG-FD method has proven to be an accurate approach to simulate the wave propagation phenomenon in porous media ([26],[23]). The geometric discretization is taken from the voxel data in section 3.2.

4.3. Water saturated aluminum foam simulation

Biot's theory ([3]) states that a wave propagating at high frequencies in a fluid saturated medium is constituted by two pressure waves and a shearing wave. Therefore it is expected that two P-waves can be measured using the first and second arrivals of the signal in the recorded data in the seismograms. It was only possible to measure a single P-wave from the seismographs, the other arrivals had excessive noise. Nevertheless, it was possible to view both propagating waves in the water saturated foam by digitally draining part of the foam and taking a snapshot when the wave was travelling through Ω_2. On Fig. 9(a), the aluminum foam phase has a faster propagating wave than that of the water phase. The measured velocity $V_{p,biot}$ is 1487 m/s.

4.4. Water saturated stiffened aluminum foam simulation

The simplification by Steeb ([28]) of Biot's equations leads to a single formula (2) where the pressure wave velocities can be calculated. All the material parameters necessary to calculate Biot-Willis' coefficients (i.e. N, A, Q, R, P and the density tensor $\hat{\rho}_{i,j}$) were measured with laboratory experiments except for the tortuosity. Therefore in order to calculate the tortuosity from the experimental setup, an additional simulation must be performed.

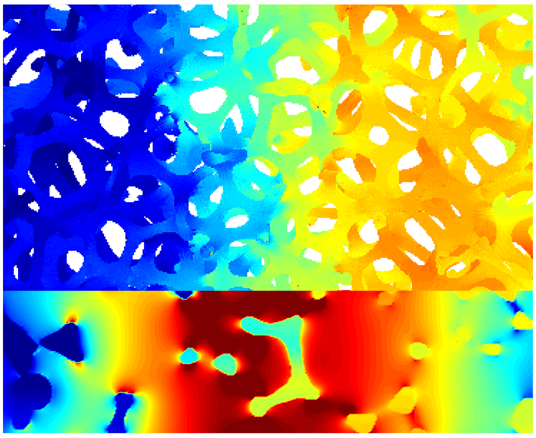

(a) Pressure wave snapshot in Ω_2. The camera is set perpendicular to the z-x plane.

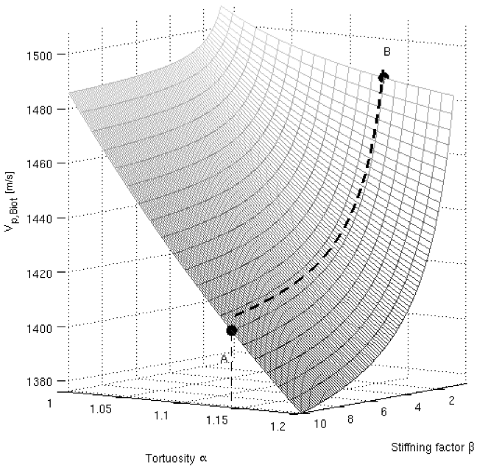

(b) Change in $V_{p,biot}$ as the aluminum foam is stiffened.

Figure 9 Pressure wave results for the stiffened and non-stiffened aluminum foam.

$$
\xi_{1,2} = \frac{\Delta \pm \sqrt{\Delta^2 - 4(PR - Q^2)(\hat{\rho}_{11}\hat{\rho}_{22} - \hat{\rho}_{12}\hat{\rho}_{12})}}{2(PR - Q^2)},
$$
$$
\Delta = P\hat{\rho}_{22} + R\hat{\rho}_{11} - 2Q\hat{\rho}_{12}. \qquad (2)
$$

To circumvent the missing P-wave velocity problem, the aluminum foam is virtually stiffened with a parameter β. The effect of the stiffening parameter on $V_{p,biot}$ can be seen on Fig. 9(b). The density and Young's modulus of aluminum foam are multiplied by this parameter. This in turn doesn't modify the P-wave modulus of the aluminum phase, but it does create a very high impedance between the solid and fluid phase. The high impedance between the phases means that the wave will be mainly traveling through the water phase, and this allows to a very clear reading of the signals at the seismographs of $V_{p,biot}$.

The measured $V_{p,biot}$ for the stiffened aluminum foam setup is 1409 m/s. When comparing both results of $V_{p,biot}$ with the variance of the stiffening parameter β, and the tortuosity, it was found that the tortuosity of the aluminum foam is $\alpha_\infty = 1.14$.

We compare our results of tortuosity with the experimental results presented by Gueven et al. in [9] and [10] ($\alpha_\infty = 1.054$), finding that they match closely. From this we can verify that the proposed geometric model of the aluminum foam represents correctly the porous material sample.

We also compare our results with the values presented in [7], where the aluminum foam is modelled with a truncated tetrahedron. We find that geometrical modelling from micro-CT data give us more accurate information about the material properties than simplified models.

5. CONCLUSIONS AND FUTURE WORK

The raw data of micro-CT data of an aluminum foam was successfully transformed from a scalar field in a regular grid in $\mathbb{R}^3$ to a watertight union of parametric surfaces $\cup_i S_i(u, w)$. From micro-CT based triangular mesh, it was possible to simulate the phenomenom of wave propagation in Biot's high-frequency domain. The parametric form of the mesh, $\cup_i S_i(u, w)$, allows to determine important geometric parameters used in Biot's equations (porosity, pore radius). Our geometric procedure was validated with simulations of wave propagation, and these closely resemble experimental results.

Future work includes the implementation of boundary elements, iso-geometrical analysis, calculation of additional macro-scale material properties and the intelligent automatic thinning of the cavernous system to achieve a graph - based node / beam representation.

ACKNOWLEDGMENT

The present work was supported by Ruhr-University, Germany, the CAD CAM CAE Laboratory, Universidad EAFIT, Colombia, and the Colombian Administration for Science and Technology (Colciencias). The authors thank Juan S. Ortiz, Jorge M. Patino and Diego Uribe for their expertise using RapidForm (TM) in the data quality control and exporting to FEA software.

References

[1] R. Adams and L. Bischof. Seeded region growing. *Pattern Analysis and Machine Intelligence, IEEE Transactions on*, 16(6):641–647, 1994.

[2] N. Amenta, S. Choi, and R. K. Kolluri. The power crust. In *Proceedings of the sixth ACM symposium on Solid modeling and applications*, SMA '01, pages 249–266, New York, NY, USA, 2001. ACM.

[3] M. A. Biot. Theory of propagation of elastic waves in a fluid-saturated porous solid. II. Higher frequency range. 29:168–191, 1956.

[4] J. Boissonnat and B. Geiger. Three-dimensional reconstruction of complex shapes based on the delaunay triangulation. pages 964–975, 1993.

[5] V. Caselles, R. Kimmel, G. Sapiro, and C. Sbert. Minimal surfaces based object segmentation. *Pattern Analysis and Machine Intelligence, IEEE Transactions on*, 19(4):394–398, 1997.

[6] M. Desbrun, M. Meyer, and P. Alliez. Intrinsic parameterizations of surface meshes. In *Computer Graphics Forum*, volume 21, pages 209–218. Wiley Online Library, 2002.

[7] J. G. Fourie and J. P. Du Plessis. Pressure drop modelling in cellular metallic foams. *Chemical Engineering Science*, 57(14):2781–2789, 2002.

[8] S. Gasser, F. Paun, and Y. Brechet. Absorptive properties of rigid porous media: Application to face centered cubic sphere packing. *The Journal of the Acoustical Society of America*, 117:2090, 2005.

[9] I. Gueven, P. Kurzeja, S. Luding, and H. Steeb. Experimental evaluation of phase velocities and tortuosity in fluid saturated highly porous media. *PAMM*, 12(1):401–402, 2012.

[10] I. Gueven, S. Luding, and H. Steeb. Hydraulic and acoustic investigation of sintered glass beads. *AIP Conference Proceedings*, 1542(1):581–584, 2013.

[11] P. Iassonov and M. Tuller. Application of segmentation for correction of intensity bias in x-ray computed tomography images. *Vadose Zone Journal*, 9(1):187–191, 2010.

[12] B. Jüttler and A. Felis. Least-squares fitting of algebraic spline surfaces. *Advances in Computational Mathematics*, 17(1-2):135–152, 2002.

[13] M. Kazhdan, M. Bolitho, and H. Hoppe. Poisson surface reconstruction. In *Symposium on Geometry Processing*, pages 61–70, 2006.

[14] P. Kurzeja and H. Steeb. About the transition frequency in biot's theory. *The Journal of the Acoustical Society of America*, 131(6):EL454–EL460, 2012.

[15] W. E. Lorensen and H. E. Cline. Marching cubes: A high resolution 3d surface construction algorithm. *SIGGRAPH Comput. Graph.*, 21(4):163–169, August 1987.

[16] M. Morse. *The Calculus of Variations in the Large*. American Mathematical Society: Colloquium publications. American Mathematical Society, 1932.

[17] W. Oh and B Lindquist. Image thresholding by indicator kriging. *Pattern Analysis and Machine Intelligence, IEEE Transactions on*, 21(7):590–602, 1999.

[18] S. Petitjean. A survey of methods for recovering quadrics in triangle meshes. *ACM Computing Surveys (CSUR)*, 34(2):211–262, 2002.

[19] A. S. Phani, J. Woodhouse, and NA Fleck. Wave propagation in two-dimensional periodic lattices. *The Journal of the Acoustical Society of America*, 119:1995, 2006.

[20] O. Ruiz, S Arroyave, D. Acosta, C. Cadavid, and J. Londono. Manifold learning for optimized fitting of freeform surfaces. In *Symposium on Geometry Processing 2013*, 2013. Submitted.

[21] O. Ruiz, C. Cadavid, M. Granados, S. Pena, and E. Vásquez. 2d shape similarity as a complement for voronoi-delone methods in shape reconstruction. *Computers & Graphics*, 29(1):81–94, 2005.

[22] O. Ruiz, C. Vanegas, and C. Cadavid. Principal component and voronoi skeleton alternatives for curve reconstruction from noisy point sets. *Journal of Engineering Design*, 18(5):437–457, 2007.

[23] E. H. Saenger. Numerical methods to determine effective elastic properties. *International Journal of Engineering Science*, 46(6):598 – 605, 2008. Special Issue: Micromechanics of Materials.

[24] E. H. Saenger, N. Gold, and S. A. Shapiro. Modeling the propagation of elastic waves using a modified finite-difference grid. *Wave Motion*, 31(1):77 – 92, 2000.

[25] E. H. Saenger and S. A. Shapiro. Effective velocities in fractured media: A numerical study using the rotated staggered finite-difference grid. 50(2):183–194, 2002.

[26] E. H. Saenger, S. A. Shapiro, and Y. Keehm. Seismic effects of viscous biot-coupling: Finite difference simulations on micro-scale. *Geophysical Research Letters*, 32(14):n/a–n/a, 2005.

[27] M. Sezgin and B. Sankur. Survey over image thresholding techniques and quantitative performance evaluation. *Journal of Electronic Imaging*, 13(1):146–165, 2004.

[28] H. Steeb. Ultrasound propagation in cancellous bone. *Archive of Applied Mechanics*, 80:489–502, 2010.

[29] J. Virieux. Velocity-stress finite-difference method. *Geophysics*, 51:889–901, 1986.

[30] O. Wirjadi. *Survey of 3d image segmentation methods*. ITWM, 2007.